Characterization of Autophagy Cargo Profiles during Starvation and Exercise with a Novel Autophagosome Isolation Method

Mohd Farhan[1], Trezze P Nguyen[1], Dakai Zhang[1], Hong Liang[1], Yong Zhou[1,2], Hongyuan Yang[1,2], Guangwei Du[1,2], Yang Liu[1,2, *]

[1]Department of Integrative Biology and Pharmacology, McGovern Medical School, University of Texas Health Science Center at Houston, Houston, Texas, 77030, USA

[2]Molecular and Translational Biology Program, MD Anderson Cancer Center UTHealth Graduate School of Biomedical Sciences, Houston, Texas, 77030, USA

[*]Corresponding author. Tel: +1 713 500 5566; E-mail: yang.liu.2@uth.tmc.edu

Keywords:

Autophagy cargo; starvation; exercise; autophagosome isolation

Abstract:

Autophagy is a cellular process to clear unwanted and dysfunctional cellular cargoes, which are sequestered in autophagosomes before their delivery to lysosomes for degradation. Autophagy cargo selection, mediated by cargo receptors, varies across cell types and conditions. Understanding the cargo features is essential for elucidating autophagy's function in specific physiological or pathological contexts. Here we present a simple and rapid method for isolating LC3B-positive autophagosomes from the tissues of GFP-LC3 transgenic mice, a widely used autophagy reporter model. When combined with quantitative proteomics, this approach enables efficient in vivo characterization of autophagy cargoes. We applied this method to establish autophagy cargo profiles in skeletal muscle during starvation and exercise-two physiological conditions that activate autophagy-and identified distinct cargo selection patterns, with significantly higher levels of ER-phagy and ribophagy observed during starvation. We further revealed the ER-phagy receptors TEX264 and FAM134B as potential mediators of the elevated ER-phagy under starvation. In summary, we report an efficient workflow for in vivo autophagy cargo characterization and provide detailed analysis and comparison of cargo profiles under starvation and exercise conditions.

Introduction:

Macroautophagy (hereinafter autophagy) is an evolutionary conserved process to degrade unwanted and dysfunctional cytoplasmic components, known as autophagy cargoes. Autophagy plays a vital role in maintaining cellular homeostasis by removing harmful intracellular materials and facilitating the reuse of internal source of nutrients under stress conditions (Levine & Kroemer, 2019). Autophagy cargoes are first engulfed by double-membrane vesicles called autophagosomes, which then deliver them to lysosomes for degradation. To date, numerous autophagy cargoes have been reported, including cytosolic proteins, protein aggregates, intracellular pathogens and nearly all the organelles (Morishita & Mizushima, 2019). As the crucial "cleaning" and "recycling" process in the cell, autophagy plays an essential role in maintaining normal cellular functions. And dysregulation of autophagy has been implicated in the pathogenesis of various diseases (Klionsky *et al*, 2021).

The initial step of autophagy involves the formation of an isolation membrane, called a phagophore, near the cytoplasmic cargo. The phagophore expands around the cargo and is ultimately sealed to form an autophagosome, with the cargo sequestered inside. The autophagosomes then fuse with lysosomes to form autolysosomes, where the cargo is degraded (Dikic & Elazar, 2018). The initiation of autophagy requires the activation of ULK1/2 kinase, Class III phosphoinositide 3-kinase (PI3K), and serial downstream events mediated by many autophagy-related proteins (Dikic & Elazar, 2018). A critical event during phagophore elongation is the conjugation of cytosolic ATG8 proteins to phosphatidylethanolamine (PE) on both sides of the phagophore membrane (Dikic & Elazar, 2018). The lipidated ATG8 proteins play essential roles in phagophore elongation and closure as well as autophagy cargo capture, and remain on both outer and inner membranes of the autophagosomes to facilitate fusion with lysosomes (Martens & Fracchiolla, 2020). After the formation of autolysosomes, ATG8 proteins on the cytosolic side of the membrane are cleaved off by ATG4 proteins (Zhang *et al*, 2016). Seven ATG8 proteins have been identified in human, categorized into two subfamilies: the LC3 family (comprising LC3A, LC3B, LC3B2, and LC3C) and the GABARAP family (including GABARAP, GABARAPL1, and GABARAPL2) (Rogov *et al*, 2023). Although all ATG8 proteins are presumed to fulfill similar functions due to structural similarities, recent studies suggest that GABARAP family proteins may play more essential roles in autophagosome formation and fusion with lysosomes, while LC3 family proteins may be more important for cargo recognition (Nieto-Torres *et al*, 2021). However, the specific roles of different ATG8 proteins in distinct cell types and their potential functional redundancy require further clarification. Among the ATG8 protein family, LC3B is the most extensively studied for its roles in autophagosome biogenesis and turnover as well as cargo recognition (Schaaf *et al*, 2016). Monitoring the lipidation of LC3B (hereafter referred to as LC3) is the most commonly employed method for assessing autophagy levels. For instance, a GFP-LC3B transgenic mouse strain (hereafter referred to as the GFP-LC3 mouse) was developed by N. Mizushima and colleagues to facilitate in vivo monitoring of autophagy (Mizushima *et al*, 2004), and has since been widely adopted by various research groups to investigate autophagy under diverse physiological and pathological conditions. In the cells of these transgenic mice, autophagosomes are decorated with lipidated GFP-LC3, and therefore can be visualized and quantified to reveal autophagy levels (Mizushima *et al.*, 2004).

The autophagy process can be non-selective and/or selective. Non-selective autophagy involves the random engulfment of cytoplasmic material into autophagosomes for degradation, while selective autophagy targets specific cargoes (Levine & Kroemer, 2019). The capture of these cargoes during selective autophagy is mediated by cargo receptors that bind to or reside on the cargoes. These receptors utilize a LC3-interacting region (LIR) to interact with lipidated ATG8 proteins on phagophores, facilitating the capture of the cargoes by phagophores and autophagosomes (Lamark & Johansen, 2021). For instance, the cargo receptor p62/SQSTM1

binds to the ubiquitinated substrates and ATG8 proteins, directing these substrates to autophagosomes (Zaffagnini *et al*, 2018). In well-studied forms of selective autophagy, such as mitophagy (the degradation of mitochondria) and ER-phagy (the degradation of the endoplasmic reticulum [ER]), multiple receptors have been identified that may function under distinct conditions and in different cell types (Ding & Yin, 2012; Mochida & Nakatogawa, 2022).

As a defense mechanism against nutrient and energy stresses, autophagy is activated during both fasting (starvation) and endurance exercise—two conditions known to confer beneficial effects on health in humans and model organisms, such as slowing down the aging process and combating age-related diseases (Escobar *et al*, 2019). Notably, autophagy activation has been shown to contribute, at least partially, to these positive outcomes (Hansen *et al*, 2008; He *et al*, 2012; Morselli *et al*, 2010). Despite the important role of autophagy during fasting and exercise, the nature of the cargoes in these two conditions remains unknown.

One primary function of autophagy is to degrade the cargoes, therefore, a thorough understanding of autophagy cargo properties under specific physiological or pathological conditions would provide mechanistic insights into how autophagy fulfills its roles. The rapid development of high-throughput omics technologies has enabled detailed characterization of organelles (Abu-Remaileh *et al*, 2017; Chen *et al*, 2016; Xiong *et al*, 2019), yet our understanding of the features of autophagosomes in vivo, including their cargoes, remains incomplete due to the lack of effective isolation methods. Conventional techniques, such as density gradient ultracentrifugation, are complex and time-consuming, requiring large amounts of starting material, which limits their feasibility (Bains & Singh, 2021). Here we introduce a simple, immunoaffinity-based method for isolating LC3B-positive autophagosomes from the tissues of GFP-LC3 mice using relatively small amounts of starting material. When combined with quantitative proteomics, this method allows the characterization of autophagy cargo in vivo. We apply this approach to establish autophagy cargo profiles in skeletal muscle during starvation and exercise, and reveal distinct cargo selection patterns under these two conditions. We anticipate that this method, along with the very first analysis and comparison of autophagy cargo features during starvation and exercise, will serve as a valuable resource for the field of autophagy research.

Results and Discussion:

Isolation of autophagosomes from the tissues of GFP-LC3 mice for downstream characterization

As a widely used autophagy reporter, the GFP-LC3 mouse strain allows for in vivo monitoring of autophagy levels (Mizushima *et al.*, 2004). GFP-LC3 is expressed at adequate levels across a variety of tissues in this mouse model (Mizushima *et al.*, 2004). The presence of lipidated GFP-LC3 on autophagosome membrane enables immunoaffinity-purification of autophagosomes using anti-GFP antibodies. Although several studies have employed this strategy (Yao *et al*, 2016; Yao *et al*, 2019), apparent caveats exist in these published methods, including the inability to assess non-specific binding of cytoplasmic components to the GFP antibody-coupled beads and visible contamination from unlipidated cytosolic GFP-LC3 in the preparations. To address these issues, we took the following approaches. First, when processing tissues from GFP-LC3 mice for autophagosome isolation, we included control tissues from wild-type (WT) mice without GFP-LC3 expression alongside. This allows us to determine the non-specific binding signals and accurately reflect the true signals coming from autophagosomes. Second, we performed size exclusion chromatography (SEC) on the tissue lysates to completely remove cytosolic GFP-LC3 (**Fig 1A and B**). Due to their larger size, autophagosomes elute in the earlier fractions during SEC, as reflected by the presence of

lipidated GFP-LC3 and LC3 (marked as II), together with other large cellular components. In contrast, the cytosolic GFP-LC3 and LC3 (marked as I) are only found in the later fractions (**Fig 1B**). Notably, lipidated GFP-LC3 and LC3 are still present in these later fractions, suggesting the existence of smaller structures containing lipidated LC3, potentially phagophores or fragmented autophagosomes. Furthermore, we observed that ATG5 and phosphorylated ATG16L1 (Ser278), markers for phagophores (Koyama-Honda *et al*, 2013; Tian *et al*, 2020), are absent from the earlier fractions and present in the later ones, providing additional evidence suggesting that the earlier fractions contain mature autophagosomes while the later fractions contain phagophores (**Fig 1B**). Thus, we collected the earlier fractions for autophagosome isolation using anti-GFP nanobody tandem-conjugated magnetic beads (see Materials and Methods for details). This workflow enabled effective purification of autophagosomes from the skeletal muscles of starved GFP-LC3 mice (both quadriceps muscles from one mouse used per isolation), as indicated by the enrichment of lipidated GFP-LC3, LC3 and p62/SQSTM1 in the isolation preparation from GFP-LC3 mice compared to that from WT control (**Fig 1C**). The isolation efficiency was approximately 50%, calculated by comparing the depletion of GFP-LC3 II after isolation to the total amount present before isolation (**Fig 1C**). Further analysis with Electron Microscope reveals double-membrane vesicles that resemble autophagosomes in the preparation (**Fig 1D**). Notably, to achieve more effective pull-down of autophagosomes within a short timeframe, we leveraged a newly developed anti-GFP nanobody tandem (Zhang *et al*, 2020) expressed and purified from *E.coli* (**Fig EV1A**), which exhibits ultra-high affinity for GFP. Compared to single GFP nanobody, the use of the nanobody tandem resulted in more effective autophagosome isolation, as evidenced by higher levels of lipidated GFP-LC3 and LC3 as well as p62 in the preparation (**Fig EV1B**).

One limitation of this isolation method is that other lipidated GFP-LC3-positive vesicles, such as phagosomes and endosomes (Pena-Martinez *et al*, 2022), may also be co-isolated with autophagosomes. A more vigorous control would involve performing the isolation in tissues with impaired autophagosome formation but intact LC3 conjugation to other membranes, such as FIP200-deficient tissues. However, achieving these conditions in mice poses significant challenges. To reduce the influence of these additional vesicles on autophagy cargo characterization, we excluded endosomes and transport vesicles from our cargo analysis, as discussed further in the section “Autophagy cargo profiles during starvation and exercise in skeletal muscle”

To test the suitability of the purified autophagosomes for cargo characterization, we conducted label-free quantitative mass spectrometry analysis to compare protein abundance in the autophagosome preparations from the skeletal muscle of a starved GFP-LC3 mouse and a WT control mouse in a proof-of-concept experiment (**Appendix Fig S1**). We identified approximately 1,160 proteins with higher abundance in the GFP-LC3 sample, including 638 proteins unique to this sample. In comparison, we identified about 670 proteins in the WT sample, highlighting the importance of including such controls to account for non-specific binding signals (**Appendix Fig S1)**. If we define “proteins from autophagosomes” as those whose abundance in the GFP-LC3 sample is at least 1.5 times more than that in the WT sample—a threshold established in previous studies using similar immunoaffinity-based strategies for lysosome purification (Wyant *et al*, 2018)—approximately 1,100 proteins meet this criterion, including dozens of known autophagosome proteins and autophagy receptors, namely LC3B, FYCO1 (Pankiv *et al*, 2010), p62/SQSTM1, NBR1 (Kirkin *et al*, 2009), FAM134B (Reticulophagy regulator 1) (Khaminets *et al*, 2015), TEX264 (An *et al*, 2019; Chino *et al*, 2019), BCL2L13 (Murakawa *et al*, 2015), PHB2 (Wei *et al*, 2017), *etc* (**Dataset EV1**).

Thus, the autophagosome isolation method proposed here represents a powerful tool for the rapid purification (in ~2.5 hours) of LC3B-positive autophagosomes from GFP-LC3 mouse

tissues using relatively small amounts of starting material (e.g., the quadriceps muscles from one mouse under starvation condition). Notably, this workflow can also be applicated to isolate autophagosomes from cell lines with GFP-LC3 expression, as evidenced by the enrichment of lipidated GFP-LC3, LC3 and p62/SQSTM1 in the isolation preparations from GFP-LC3 expressing cells compared to control cells (**Fig EV2**; tested in HeLa and MIA PaCa2 cell lines), further expanding its application. When combined with quantitative omics, this method enables accurate assessments of autophagosome contents and other characteristics.

Autophagy cargo profiles during starvation and exercise in skeletal muscle

Fasting (starvation) and exercise are two major physiological conditions that activate autophagy, which helps recycle intracellular nutrients in response to the nutrient/energy stresses under these two conditions. Both starvation and exercise induce autophagy in various tissues of mice, including skeletal muscle, cardiac muscle, liver, pancreas, *etc* (He *et al.*, 2012; Mizushima *et al.*, 2004). While autophagy activation induced by nutrient/energy stresses was initially thought to be non-selective, growing evidence suggests that during bulk autophagy, some cargoes (such as cytosolic proteins) are engulfed into autophagosomes in a non-selective way, while others are selectively targeted to autophagosomes through cargo receptors (Lamark & Johansen, 2021). For example, during starvation in cell lines, ER and ribosomes can be specifically chosen for autophagic degradation through the actions of ER-phagy receptors and ribophagy receptor, respectively (An *et al.*, 2019; Chino *et al.*, 2019; Wyant *et al.*, 2018). In addition, it has been shown that mitophagy is activated by exercise in skeletal muscle, although the responsible receptor(s) remain unclear (Guan *et al*, 2019). Despite these understandings, a comprehensive analysis of autophagy cargoes in mouse tissues under starvation and exercise conditions is lacking. Therefore, we applied the workflow described above to address this knowledge gap.

In this study, we focused on skeletal muscle because a dramatic increase in autophagy levels following moderate-intensity aerobic exercise was observed in this tissue (He *et al.*, 2012; Liu *et al*, 2020) and relatively large amount of material can be obtained from a single mouse. For researchers interested in applying the described workflow to isolate autophagosomes from tissues other than skeletal muscle, the required amount of starting material will need optimization. The quantity should be sufficient to yield enough autophagosomes for characterization without being excessive, as larger amounts may lead to increased non-specific binding, as evidenced in the WT control samples.

We first assessed the levels of lipidated GFP-LC3 II in the autophagosome-containing SEC fractions of skeletal muscle lysates from mice subjected to starvation, exercise, or left unmanipulated (basal condition), which reflect the abundance of autophagosomes. As expected, both starvation and exercise significantly increased GFP-LC3 II levels compared to the basal condition, with approximately 1.9-fold and 1.8-fold increases, respectively (**Fig EV3A**). Based on these results, in order to isolate equivalent amounts of LC3 II positive autophagosomes, we used the quadriceps muscles from one mouse for the starvation or exercise condition, while combined the quadriceps muscles from two mice for the isolation in basal condition. Compared to those from WT control mice, the autophagosomes preparations from GFP-LC3 mice in all three conditions showed enrichment of GFP-LC3 II, LC3 II and p62/SQSTM1 (**Fig EV3B**).

We then performed label-free quantitative proteomics to analyze the amounts of proteins identified in the autophagosome preparations from the three conditions. We conducted four biological replicates for each condition, and we defined proteins as “from autophagosomes” in each replicate based on a criterion that the protein’s abundance in the GFP-LC3 sample is at least 1.5-fold greater than in the corresponding WT control sample (**Dataset EV1**). We then

sought the common proteins identified in all four replicates of one condition that are significantly more abundant in the GFP-LC3 samples compared to WT control, and found 272 proteins in basal condition, 515 proteins in starvation condition, and 365 proteins in exercise condition (**Fig 2A; Dataset EV1**). To establish the autophagy cargo profiles in each condition, we next analyzed the cellular components to which these proteins belong using subcellular localization information from the Uniprot database **(Dataset EV1**). Next, we employed two analytical approaches to reflect autophagy cargo selection patterns under different conditions. In the first analysis, we calculated the total number of proteins from different cytoplasmic components-including mitochondria, cytosol, plasma, membrane, nucleus, ER (or SR [Sarcoplasmic Reticulum] in muscle), Golgi, ribosomes, peroxisomes and lipid droplets-and determined the percentage of proteins from each cytoplasmic component relative to the total number of proteins in each condition (**Fig 2B; Dataset EV1;** proteins that are localized to multiple components are counted for each of their respective localizations**)**. We excluded endosome, transport vesicle and lysosome from this analysis, as it is challenging to tell whether the proteins localized to these compartments are autophagy cargos or merely present on the membranes of autolysosomes and other GFP-LC3 II-positive vesicles, which may be co-isolated in the autophagosome preparation. We found that there are both larger number and higher percentage of proteins from mitochondria or peroxisome in the autophagosomes from exercise condition compared to the control or starvation condition, and larger number and higher percentage of proteins from plasma membrane, ER and ribosome in the autophagosomes from starvation condition compared to the control or exercise condition (**Fig 2B)**. In the second analysis, we calculated the total abundance of proteins (normalized to the abundance of LC3B in each sample) from different cellular components **(Fig 2C; Dataset EV1;** proteins that are localized to multiple components are counted for each of their respective localizations.**)**. Assuming that the same number and set of proteins from a specific cellular part was identified in the autophagosomes from two different conditions, if the abundance of these proteins is higher in one condition than the other, this still suggests higher amounts of the specific cellular part are targeted for autophagic degradation in this condition. Thus, we believe that this analysis method, which calculates not only the number but the abundance of proteins from different cellular components in the autophagosome preparations, could accurately reflect on the autophagy cargo selection patterns in different conditions. We found that in both basal and exercise conditions, proteins from mitochondria are most abundant in autophagosomes, followed by proteins from cytosol and plasma membrane (**Fig 2C**)**.** In the exercise condition, there was a significant increase in the abundance of proteins from the plasma membrane and ER compared to the basal condition. There was also a trend indicating higher abundance of peroxisomal and nuclear proteins in the exercise condition compared to the basal condition (p=0.051 and p=0.071, respectively) (**Fig 2C**). In addition, while there were larger number of mitochondrial proteins identified in the exercise condition than in the basal condition (**Fig 2B**), no significant increase in the abundance of these proteins was observed, despite a trend toward higher (p=0.15; **Fig 2C**). A possible explanation is that mitophagy is most active during the recovery period post-endurance exercise, not immediately after exercise (Laker *et al*, 2017). In starvation condition, ER (SR) proteins are the most abundant in autophagosomes, with levels drastically higher than those in both basal and exercise conditions (**Fig 2C**). Among the SR proteins identified in the autophagosomes from starvation condition, several Ca^{2+} handling molecules, namely SERCAs (Sarcoplasmic/endoplasmic reticulum calcium ATPase 1 to 3) and Calsequestrin-1 were highly abundant (together constituting approximately 30% of the total protein abundance in the autophagosome preparations), and are absent in the autophagosomes from basal and exercise conditions (**Fig EV4; Dataset EV1**). This suggests a potential preference for targeting these molecules or ER subdomains containing them for autophagic degradation during starvation in skeletal muscle. Given the extreme high abundance of these SR proteins, potential false-positive identification of them in starvation condition or false-

negative identification in basal or exercise conditions would greatly impact the analysis results. To mitigate the risk, we also analyzed the abundance of other ER proteins, excluding SERCAs and Calsequestrin-1, in the autophagosomes from starvation condition, and found that their levels remained significantly higher than those in autophagosomes from basal or exercise condition (**Fig EV4**)**.** Based on these results, we concluded that autophagosomes in starvation condition contained a greater abundance of ER proteins compared to those in basal or exercise condition. Additionally, we observed a significantly higher abundance of ribosomal proteins in the autophagosomes from the starvation condition compared to both the basal and exercise conditions in which no ribosomal proteins were identified (**Fig 2B, C**)**.** Autophagosomes from starvation condition also contained significantly higher abundance of proteins from cytosol, plasma membrane and nucleus than those from basal condition, while showing a significantly lower abundance of peroxisomal proteins compared to those from exercise condition (**Fig 2C**). Notably, there was also a trend suggesting that the abundance of mitochondrial proteins was lower in autophagosomes from starvation compared to those from exercise condition (p=0.09; **Fig 2C**). Based on our findings from the two different analyses comparing starvation and exercise conditions, we conclude that autophagosomes from the starvation condition contain dramatically higher amount of ER and ribosomes compared to those from the exercise condition. In contrast, the exercise condition showed significantly more proteins from peroxisomes and a trend towards more mitochondrial proteins in the autophagosomes compared to the starvation condition, although these differences were not as pronounced as those seen for ER and ribosomal proteins.

We next investigated whether the dramatically higher abundance of ER and ribosomal proteins in autophagosomes from starvation condition was simply a result of more ER and ribosomes available for autophagic degradation in the muscle cells during starvation. To address this, we performed label-free quantitative proteomics to analyze the abundance of proteins in the total tissue lysates from all three conditions, using three replicates for each condition. We identified common proteins across all replicates and found 474 proteins in basal condition, 471 proteins in starvation condition, and 493 proteins in exercise condition (**Fig EV5A; Dataset EV2**). Next, using these common proteins, we calculated the abundance of proteins from different cytoplasmic parts (total protein abundance considered as 100 in each sample; **Fig EV5B; Dataset EV2**). No significant differences in the abundance of proteins from ER and ribosomes were observed across the three conditions (**Fig EV5B)**. These results suggested that the higher abundance of ER or ribosomal proteins in the autophagosomes from starvation condition is likely due to enhanced selective targeting of these components for autophagic degradation. Since ER-bound ribosomes, which may account for up to 50% of total ribosomes (Reid & Nicchitta, 2012; Schreml & Burka, 1968), can be degraded along with ER via autophagy (Chino *et al.*, 2019), and considering that the only known ribophagy receptor, NUFIP1 (Wyant *et al.*, 2018), was not identified in the autophagosome preparations from starvation condition, it is possible that the increased ribophagy observed during starvation is at least partially attributable to the enhanced ER-phagy. Further investigation is needed to explore this possibility. In summary, we analyzed the autophagy cargo profiles in basal, starvation and exercise conditions in mouse skeletal muscle, and revealed distinct autophagy cargo selection patterns with dramatically higher levels of ER-phagy and ribophagy during starvation. To our knowledge, this study is the first to thoroughly examine and compare autophagy cargos in vivo during starvation and exercise, and the results suggested that even though both conditions induce general autophagy (bulk autophagy) in response to the nutrient/energy stress, there are certain differences in cargo selection patterns between the two.

Potential contribution of TEX264 and FAM134B to the elevated ER-phagy during starvation

Given the dramatic differences in ER-phagy observed between starvation and exercise conditions, we conducted additional experiments to investigate the underlying mechanisms and the potential cargo receptors involved. To date, several ER-phagy receptors have been discovered in mammalian cells, including FAM134B (also known as RETREG1/Reticulophagy regulator 1), TEX264, Sec62, RTN3L, CCPG1, *etc* (Mochida & Nakatogawa, 2022). To gain further insights into the potential mechanisms of the differential regulation of ER-phagy during starvation and exercise, we checked the presence of ER-phagy receptors in the autophagosome preparations from both conditions. We found that FAM134B, TEX264 and RTN3 are present in the autophagosomes from starvation conditions but not in those from exercise condition (**Dataset EV1**). Given this distinction, we chose to further explore the potential roles of FAM134B and TEX264 in the differential regulation of ER-phagy during starvation and exercise. We opted not to pursue RTN3 because only the full-length form of RTN3, RTN3L, contains the LIR domains and functions as an ER-phagy receptor (Grumati *et al*, 2017), however, this isoform has very weak expression in skeletal muscle (Cai *et al*, 2005). Indeed, none of the RTN3 peptides identified in our MS experiments are mapped to the specific region of RTN3L (**Appendix Table S1**). To confirm the functional roles of FAM134B and TEX264 as ER-phagy receptors, we then examined their interaction with lipidated GFP-LC3 II. Using co-immunoprecipitation assays, we observed that FAM134B interacted with GFP-LC3 II and the binding was significantly stronger in starvation condition than in exercise condition (**Fig 3A and B**). Similarly, we detected a markedly increased binding of GFP-LC3 II to TEX264 during starvation versus exercise (**Fig 3C and D).** These results indicate that both FAM134B and TEX264 likely contribute to the elevated levels of ER-phagy observed in skeletal muscle during starvation. Our findings align with previous studies using cell line models demonstrating that TEX264 is the major ER-phagy receptor which contributes to at least 50% of the total ER-phagy during starvation (An *et al.*, 2019; Chino *et al.*, 2019), and that FAM134B also contributes to starvation-induced ER-phagy (Chino *et al.*, 2019). We recognize that the involvement of different ER-phagy receptors during starvation may vary across different tissues, which requires further clarification in future studies.

In summary, here we present a novel method for isolating LC3B-positive autophagosomes from the tissues of GFP-LC3 transgenic mice, enabling in vivo characterization of autophagosome properties, including cargo features. This method allowed us to uncover distinct autophagy cargo selection patterns in skeletal muscle during starvation and exercise, underscoring the complexity of autophagy regulation in response to various stressors.

Materials and Methods:

Mouse strains

All mice were housed in the Center for Laboratory Animal Medicine and Care (CLAMC) at University of Texas Health Science Center at Houston under 12-h light–dark cycles with ad libitum access to food and water. All the experimental procedures related to mouse were approved by the institutional Animal Welfare Committee (AWC) and performed in accordance with institutional guidelines. Twelve- to sixteen-week-old male mice were used. GFP-LC3B transgenic mouse strain (Mizushima *et al.*, 2004) was a kind gift from Dr. Noboru Mizushima and has been backcrossed with C57BL/6J mice for at least five generations. Wild-type (WT) and GFP-LC3B mice (heterozygous for GFP-LCB transgene) used in the experiments were littermates generated from the breeding between WT and heterozygous GFP-LC3B mice.

Plasmids

Plasmid that expresses single GFP nanobody (GBP1/Enhancer) was a gift from Dr. Rebecca Voorhees (Addgene plasmid # 149336; http://n2t.net/addgene:149336; RRID:

Addgene_149336). A tandem GFP nanobody (GBP1/Enhancer+ LaG16) was describe in a previous study (Zhang *et al.*, 2020). Plasmid that contains tandem GFP nanobody sequence was a gift from Dr. Motoyuki Hattori (Addgene plasmid # 140442; http://n2t.net/addgene:140442; RRID: Addgene_140442). The plasmid that expresses tandem GFP nanobody (GBP1/Enhancer+ LaG16) was generated by replacing the GBP1/Enhancer sequence in the single nanobody vector with the tandem nanobody sequence using Gibson assembly. Notably, sequences expressing the His14 tag, an Avi tag and a $SUMO^{EU1}$ tag (can be cleaved by a $SENP^{EuB}$ protease) are present in front of the nanobody sequence (discussed in the section "Preparation of GFP nanobody-conjugated magnetic beads" below). Plasmid contains GFP-LC3B (R. norvegicus) sequence was a gift from Dr. Noboru Mizushima (Addgene plasmid # 38195; http://n2t.net/addgene: 38195; RRID: Addgene_38195). Lentiviral vector (backbone: pLenti-IRES-Neo) that contains the GFP-LC3B (R. norvegicus) sequence was generated using Gibson assembly.

Cell culture

Phoenix, HeLa and MIA Paca-2 cells were from and pre-authenticated by ATCC and used at low passage (<10) number. All cell lines were tested negative for mycoplasma contamination by PCR analysis at biweekly intervals throughout the study. All cell lines were cultured in DMEM (Sigma, D6429) containing 10% FBS (Sigma, F2442), 2 mM L-glutamine (Sigma, G7513) and non-essential amino acids (Sigma, M7145). Lentiviruses carrying GFP-LC3B sequence (or empty as control) were packaged in Phoenix cells by co-transfection of lentiviral vectors with packaging plasmids using Lipofectamine 2000 (Invitrogen, 11668019). Media containing virus particles were collected 48 h after transfection and used for infecting target cells for 4 h in the presence of 8 μg/ml polybrene. Forty-eight hours after infection, neomycin was added to the medium of the infected cells for selection, and the cells were used for experiments once the selection was over.

Starvation and exercise in mice

For starvation condition, mice were put into a new cage without food with water around 4:00 pm the day before experiment, and maintained in the cage for 18 hours (till 10:00 AM next day) before being euthanized for tissue collection. For basal condition, after the mice underwent an 18-hours starvation as describe above, food was added back to the cage to refeed the mice for 4 to 5 hours before being euthanized for tissue collection.

For exercise condition, treadmill running in mice were performed as previously described (Liu *et al.*, 2020) with minor modifications. In brief, mice were acclimated to the 10° uphill treadmill for two days. On day 1, mice ran for 5 min at a speed of 8 m/min followed by 2 min at a speed of 10 m/min. On day 2, mice ran for 5 min at a speed of 10 m/min followed by 2 min at a speed of 12 m/min. On day 3 and 4, mice were allowed to rest. Around 4 :00 pm on day 4, food was removed from the cages and the mice were starved for 18 hours. In the morning of day 5, food was put back into the cages to refeed the mice for 4 hours before the exercise experiment. Mice were subjected to a single bout of running starting at a speed of 10 m/min for 40 min. Afterwards, the speed was increased at a rate of 1 m/min every 10 min for a total of 30 min and then at a rate of 1 m/min every 5 min until finishing 18 m/min (total 95 min) when the mice were euthanized, and tissues were collected.

GFP nanobody purification

The single or tandem GFP nanobody protein was expressed in NEBExpress® I^q *E. coli* (New England Biolab, C3037I) as described previously (Pleiner *et al*, 2020). Briefly, an 80 ml pre-culture of the *E. coli* containing the expression plasmid was grown in Super Broth (Research Products International, S33050) overnight at 28˚C and diluted to 800 ml Super Broth the next

morning. After dilution, the culture was incubated at 18˚C until reaching OD600 value around 0.9 (normally in 4 to 5 hours). The expression of the protein was then induced by addition of 0.2 mM IPTG for 18 to 20 hours at 18˚C. Cells were harvested by centrifugation and the pellet was resuspended in 70 ml lysis buffer (20 mM Hepes pH 7.5, 300 mM NaCl, 20 mM imidazole, 1 mM DTT, 1 mM PMSF) and lysed by a French press. The lysate was cleared by centrifugation for 45 min at ~35,000 *g* at 4˚C. The supernatant was then incubated with 1.5 ml bed volume Ni^{2+}-NTA resin (Thermo Scientific, 88221), which has been equilibrated to lysis buffer, for 1 hour at 4˚C before transferred to a gravity flow column. The resin was then sequentially washed with three column volume (CV) lysis buffer, 10 CV wash buffer A (20 mM Hepes pH 7.5, 300 mM NaCl, 50 mM imidazole, 1 mM DTT), 10 CV wash buffer B (20 mM Hepes pH 7.5, 300 mM NaCl, 100 mM imidazole, 1 mM DTT), and then eluted with elution buffer (20 mM Hepes pH 7.5, 300 mM NaCl, 500 mM imidazole, 1 mM DTT, 250 mM sucrose). Fourteen fractions of elution with 0.5 ml per fraction were collected and the presence of GFP nanobody in each fraction was determined by SDS-PAGE using the Mini-PROTEAN TGX stain-free precast gels (Bio-Rad, 4568096). The five fractions with the highest concentration of GFP nanobody were combined (final volume around 2.5 ml), and the buffer was then exchanged to storage buffer (20 mM Hepes pH 7.5, 200 mM NaCl, 1 mM DTT and 250 mM sucrose) using a PD-10 desalting column (GE Healthcare, 17085101) according to the user instructions. After determining the final protein concentration, the purified nanobody was aliquoted, snap-frozen in liquid nitrogen, and stored at -80˚C until further use.

Preparation of GFP nanobody-conjugated magnetic beads

Before performing the autophagosome isolation experiments, GFP nanobody protein was conjugated to NHS-activated magnetic beads (Thermo Scientific, 88827). For each 100 µl beads, 120 µg tandem GFP nanobody (or 80 µg single nanobody) was used for conjugation. The conjugation steps were performed according to the user guide of the beads except that different coupling buffer (20 mM Hepes pH 7.5, 200 mM NaCl) and storage buffer (KPBS [potassium phosphate-buffered saline] with 2 µg/µl BSA) were used. The prepared beads can be stored at 4˚C for a week before usage.

Notably, the GFP nanobody used in this study has three tags at the N terminus, a His14 tag for purification, an Avi tag that can be biotinylated by the biotin ligase BirA, and a $SUMO^{EU1}$ tag that can be cleaved by a $SENP^{EuB}$ proteinase. We have tried several strategies for nanobody/beads coupling before we decided to use the current one. We first tried to biotinylate the Avi tag and couple the nanobody to streptavidin beads. However, although the coupling of nanobody to beads was very effective, we found high levels of proteins nonspecifically bound to the prepared beads during the autophagosome isolation step. We also tried using $SENP^{EuB}$ proteinase (which cut $SUMO^{EU1}$) to cleave off the nanobody together with the bound autophagosomes to reduce the nonspecific binding, however, the efficiency of releasing autophagosomes from the beads was very low, possibly due to that each autophagosome have many GFP-LC3 molecules that can bind many GFP-nanobody molecules on the beads. We noticed that when GFP nanobody protein was coupled to NHS-activated beads as described above, the nonspecific binding of proteins to the beads during autophagosome isolation step was much lower compared to the streptavidin beads. The conjugation of protein to the NHS beads relies on the formation of stable amide linkages between the primary amine from the protein and NHS on the beads. Primary amine exists at the N terminus of the protein as well as the side chain of lysine residues. There are multiple lysine residues in the Avi tag and $SUMO^{EU1}$ tag in front of the nanobody, which provides conjugation sites, and the conjugation to these sites

possibly ensures the good flexibility and accessibility of the GFP nanobody for autophagosomes binding. We tried to simplify the GFP nanobody by removing the Avi tag and SUMO[EU1] tag which are not in use and substituting with ten lysine residues separated by linker sequence (GS or GGS) to provide the conjugation sites, however, the autophagosome isolation efficiency was much lower using NHS beads conjugated with this modified nanobody, possibly because that the flexibility of nanobody on the beads was too low to effectively bind to bulky autophagosomes.

Preparation of SEC (Size Exclusion Chromatography) column

To pack SEC columns, 15 ml (dry matrix volume) of Sepharose 2B-CL matrix (Sigma, CL2B300) was added into an empty gravity column (Bio-Rad, 7321010) with caution to avoid air bubbles trapped in the matrix. A porous 30 µm polyethylene upper bed support was added on top of the matrix to retain the matrix particles. After the liquid flew though, 15 ml (1 column volume or 1 CV) 20% ethanol was added to the column, and then another 1 CV 20% ethanol was added before the column was closed for long-term storage at 4˚C. Before the usage for autophagosome isolation, the column was washed three times with 1 CV KPBS each time. For each wash, the liquid was allowed to pass through the column completely before new KPBS was added for the next wash. After the three washes, the column is fully equilibrated with KPBS and ready to be used in the isolation experiments. If the column is not used immediately after wash, 1 to 2 ml of KPBS was added to the column after the third wash to prevent the column from drying following which the column was closed and stored at 4˚C for short period of time (one or two days). Right before loading the sample (tissue or cell lysate; see the section "autophagosome isolation from tissues and cells") onto the column, let the KPBS solution completely drain through. After usage, the column should be washed three times (1 CV/wash) with Milli-Q H_2O to flush off everything from the sample, and then one time with 1 CV 0.5 M NaOH and another three times with Milli-Q H_2O. At last, the column was washed one time with 1 CV 20% ethanol, and then another 1 CV 20% ethanol was added before the column was closed for long-term storage at 4˚C. Notably, the column can be re-used multiple times if properly cleaned after each usage.

Autophagosome isolation from tissues and cells

For autophagosome isolation from GFP-LC3 mouse skeletal muscles, both quadricep muscles from one mouse were removed and briefly washed in 5 ml cold KPBS. The muscles were then padded dry on tissue paper, and each muscle was put into 900 µl cold isolation buffer (KPBS + proteinase inhibitors+ phosphatase inhibitors) in a 2 ml centrifuge tube. The muscle was diced into small pieces by scissor cutting (70 to 100 times). The buffer containing tissue pieces of both muscles were poured together into a prechilled glass douncer tube (3 ml capacity; to be used with motor-driven pestle later; DWK Life Sciences, 886000-0020). Another 700 µl of cold isolation buffer was used to wash the two centrifuge tubes sequentially to get the remaining tissue pieces, and this washing buffer was also added into the douncer tube (total ~ 2,500 µl isolation buffer in the tube). Attach the pestle to the motor-drive homogenizer (Glas-Col, 099CK54), and push the pestle into the douncer tube containing the tissue pieces until it cannot go further. Turn on the motor (turning clockwise at a speed ~2000 rpm), slowly push the pestle to the bottom of the douncer tube before slowly pulling the pestle up till it reaches the surface of the liquid (considered as stroke 1). Perform 10 strokes at room temperature during which time the disperse of the tissue can be monitored clearly, then perform an additional 15 strokes on ice. Put the douncer tube on ice, meanwhile, get any big tissue pieces stuck on the pestle and put them back into the douncer tube. Tough tendons tend to be stuck at the bottom of the douncer

tube and should be taken out for better homogenization of the tissues. Perform another 25 strokes on ice and then pour the lysate evenly into two prechilled 1.5 ml centrifuge tubes. Please note that the homogenization procedure described here is optimized for skeletal muscle, which is hard to break; for other softer tissues, it may not be necessary to perform as many strokes as for skeletal muscle to generate the tissue lysate. After homogenization, the crude tissue lysates in the two centrifuge tubes were centrifuged three times at 700 *g*, 4˚C for 5 min each time to get rid of any tissue debris. After the last centrifugation, pour the supernatant from the two tubes together to get the final tissue lysate (~1.5 to 1.7 ml). Load the tissue lysate onto the SEC column prewashed with KPBS as described in the previous section, and start collecting the 4.5 ml void volume. During this time, when the lysate completely passed through, add ~7 to 8 ml of cold KPBS onto the column. After collecting the void volume, 3 ml elute that contains the majority of mature autophagosomes is collected. Please note that the void volume and elution volume were pre-determined for specifically using 15 ml column matrix and ~1.5 ml lysate. During the pre-determination process, 0.5 ml fraction were collected sequentially, and the presence of autophagosome or phagophore marker proteins were determined in each fraction by western blots. If the column volume or/and lysate volume changes, the optimal void volume and elution volume will change and need to be determined again. Once obtained the 3 ml elute that contains autophagosomes, BSA (final concentration 2 μg/μl), proteinase inhibitors and phosphatase inhibitors are added to the elute before 150 ul GFP-nanobody conjugated NHS-activated magnetic beads (the preparation was described in the related section above) are added. Incubate the mixture for 30 min on a rotator at 4˚C before the beads were washed five times with cold KPBS. After the wash, beads can be resuspended in the buffer of choice for downstream analysis. For western blots and label-free quantitative Mass Spectrometry in this study, 50 μl of 2×Laemmili buffer was used to resuspend the beads. The beads were then incubated for 15 min at 37 ˚C with occasional mixing before the supernatant was taken for further analysis. Notably, the addition of BSA during isolation step can reduce the non-specific binding of proteins to the beads. For autophagosome isolation during starvation and exercise, quadricep muscles (both) from one GFP-LC3 mouse was sufficient to obtain enough autophagosomes for downstream analysis. For autophagosome isolation during basal condition, quadricep muscles (both) from two GFP-LC3 mice were used, in which case the SEC elute from the two mice were combined together (total 6 ml) before 150 ul GFP-nanobody conjugated beads were added to carry out the later steps as described above. Notably, when performing autophagosome isolation from GFP-LC3 mice, muscles from WT mice subjected to the same treatment are processed at the same time in the same way to be used as non-specific binding controls.

For autophagosome isolation from GFP-LC3 expressing HeLa and MIA Paca-2 cells, four 10 cm dishes with 2 million cells per dish were used. The cells were starved with EBSS for 2 hours in the presence of 50 nM Bafilomycin A1 (a lysosome inhibitor) before the cells were washed one time with cold KPBS and scraped into ~ 1.6 ml cold isolation buffer (400 ul per dish; isolation buffer described in the previous paragraph). Cells were lysed using prechilled Isobiotec cell homogenizer (Isobiotec), during which process the cells plasma membrane broke due to being forcibly pushed through a narrow gap formed between the ball of choice and chamber walls of the homogenizer. The clearance of the gap can be adjusted by using a ball with different diameters, and different cell lines may require different clearances as well as different number of times of passing-through to effectively break the plasma membrane but maintain the membranes of intracellular organelles intact. For both HeLa cells and MIA Paca-2 cells, a clearance of 14 μm and five times of passing-through the chamber were used to lyse the cells.

After homogenization, the crude cell lysates were centrifuged three times at 700 *g*, 4˚C for 5 min each time to get rid of any cell debris. The obtained final cell lysates (~1.5 to 1.7 ml) were then subjected to the downstream SEC and pull-down procedures using the same protocol as for tissues, except that 100 ul GFP-nanobody conjugated beads were used for autophagosome pull-down.

Label-free proteomic and data analysis

The autophagosome preparations (in 2×Laemmili buffer) or 10 µg total tissue lysates (in 2×Laemmili buffer) were run into 4–20% precast gel (Bio-Rad, 4561094) for around 1 cm distance. The gel was then stained with GelCode™ Blue Stain (Thermo Scientific, 24590) briefly before destained thoroughly with ultrapure water to visualize the areas containing proteins. Those areas were cut-off from the gel and briefly rinsed with 50% acetonitrile in water. The gel slices were subsequently cut into 1×1 mm pieces and subjected to in-gel digestion using trypin as described previously (Shevchenko *et al*, 2001).

An aliquot (around a quarter) of the tryptic digest (in 2 % acetonitrile/0.1% formic acid in water) was analyzed by LC/MS/MS on an Orbitrap Fusion™ Tribrid™ mass spectrometer (Thermo Scientific) interfaced with a Dionex UltiMate 3000 Binary RSLCnano System. Peptides were separated onto an analytical C18 column (100 µm ID x 25 cm, 5 µm, 18Å Reprosil-Pur C18-AQ beads from Dr Maisch, Ammerbuch-Entringen, Germany) at a flow rate of 350 nl/min. Gradient conditions were: 3%-22% B for 90 min; 22%-35% B for 10min; 35%-90% B for 10 min; 90% B held for 10 min (solvent A, 0.1 % formic acid in water; solvent B, 0.1% formic acid in acetonitrile). The peptides were analyzed using data-dependent acquisition method. Orbitrap Fusion was operated with measurement of FTMS1 at resolutions 120,000 FWHM, scan range 350-1500 m/z, AGC target 2E5, and maximum injection time of 50 ms. During a maximum 3 second cycle time, the ITMS2 spectra were collected at rapid scan rate mode, with HCD NCE 34%, 1.6 m/z isolation window, AGC target 1E4, maximum injection time of 35 ms, and dynamic exclusion was employed for 20 seconds.

The raw data files were processed using Thermo Scientific™ Proteome Discoverer™ software version 1.4. Spectra were searched against the Uniprot-mouse database using Sequest. Search results were trimmed to 1% FDR for strict and 5% for relaxed condition using Percolator. For the trypsin, up to two missed cleavages were allowed. MS tolerance was set 10 ppm; MS/MS tolerance 0.6 Da. Carbamidomethylation on cysteine residues was used as fixed modification; oxidation of methione as well as phosphorylation of serine, threonine was set as variable modifications.

Further analysis of the results was done using Microsoft Excel 2019 and GraphPad Prism 10. For each pair of samples (preparations from GFP-LC3 and WT control mice), the proteins whose abundance (the intensity of the corresponding MS spectrum) was at least 1.5 times more in the GFP-LC3 preparation than that in WT control preparation was considered “from autophagosomes”. The common proteins “from autophagosomes” were identified in the four replicates, and only the ones whose abundance are significantly higher in the GFP-LC3 preparations compared to the related WT preparations ($p \leq 0.05$ determined by paired Student’s t-test) were picked for further analysis. For proteins that were found only in GFP-LC3 samples but not the WT samples, the abundance value was set as 10^4 (the minimal detection limit) for statistical analysis. The subcellular localization of these proteins was assigned based on the information in Uniprot database. Occasionally, the subcellular localization was further confirmed and modified based on the information obtained via manually searching through literatures. Proteins that are localized to multiple components were counted for each of their respective

localizations. To calculate the relative abundance of the proteins in each condition, the original intensity value of each protein was divided by the molecular weight of the protein, and the obtained value was further normalized based on the value of LC3B in the same sample or total protein abundance (refer to the Figure legends). After normalization, the values of all the proteins with the same subcellular localization were added together to reflect the total abundance of proteins from the specific cellular compartment.

Western blots

All the primary antibodies and secondary antibodies used for western blots were purchased from commercial sources. Anti-GFP antibody (A-6455) was from Invitrogen. Anti-LC3B antibody (NB100-2220) was from Novus Biologicals. Anti-FAM134B (21537-1-AP) and anti-TEX264 (25858-1-AP) antibodies were from Proteintech. Anti-p62/SQSTM1 (P0067) and anti-Calnexin (C4731) antibodies were from Sigma. anti-ATG5 antibody (12994) was from Cell Signaling Technology. Anti-phospho-ATG16L1 Ser278 (ab195242) was from Abcam. Secondary antibodies used in the study include HRP conjugated anti-rabbit IgG antibody (SA00001-2; for regular western blots) and HRP conjugated anti-rabbit IgG (light chain specific) antibody (SA00001-7L; for immunoprecipitation samples) were from Proteintech. MINI-PROTEAN TGX stain-free precast gels (4-20%; Bio-Rad, 4568096) were used for all the experiments.

Co-immunoprecipitation

To determine the interaction between FAM134B or TEX264 with GFP-LC3 II during starvation and exercise, the SEC elute (3 ml) was obtained after the tissue lysate preparation and SEC elution as described above in the section of “Autophagosome isolation from tissues and cells”. BSA (2 μg/μl), proteinase inhibitors and phosphatase inhibitors were added into the elute before 1% Triton X-100 (v/v) was added to release proteins into the solution. For GFP-LC3 II immunoprecipitation, 75 μl single nanobody conjugated magnetic beads were added and the mixture was incubated for 30 min at 4˚C before the beads were washed five times with KPBS+1% Triton X-100. For TEX264 immunoprecipitation, 3 μg of anti-TEX264 antibody (Proteintech, 25858-1-AP) and 30 μl pre-washed Protein G Dynabeads were added to the elute and the mixture was incubated for 2 hours at 4˚C before the beads were washed five times with KPBS+1% Triton X-100. After the final wash, 50 μl of 2×Laemmili buffer was used to resuspend the beads. The beads were then incubated for 15 min at 55˚C with occasional mixing before the supernatant was taken for further analysis.

Electron Microscopy

To visualize the purified autophagosomes using Electron Microscope (EM), after performing the autophagosome isolation steps as described above, instead of using 2×Laemmili buffer to resuspend the beads, the beads were resuspended in 50 μl 100 mM trimethylamine (pH 11.8) and incubated for 5 min at room temperature before 5 μl of 1M MES (pH 3.0) were added to neutralize the solution. This pH shift causes autophagosomes dissociation from the nanobody and release into the solution. Approximately 10 μl the autophagosome-containing solution was pipetted onto a copper EM grid pre-coated with pioloform and poly-l-lysine. Solution on the grid was blotted off with a filter paper following 15 minutes of incubation. EM grid was then fixed with 4% paraformaldehyde (PFA) and 0.1% glutaraldehyde for 10 minutes, followed with blocking with 10% BSA and 1% fish skin gelatin for 20 minutes. The grids were washed four times with distilled water before embedding in methyl cellulose containing 3% uranyl acetate for negative staining. EM grids were imaged using transmission EM (TEM, JEM-1400, JEOL, USA) at

150,000X magnification. Electron micrographs were acquired using Gatan Orius SC1000A1 digital camera (Gatan) with a software of Gatan DigitalMicrograph (License ID: 165642147, Architecture: 32-bit, Version 2.02.800.0).

Data analysis

Graphs were made using GraphPad Prism 10. Statistical analysis to compare the differences between conditions were performed using two-sides, unpaired Student's t-test either in Microsoft Excel or GraphPad Prism 10.

Data Availability

The mass spectrometry data from this study have been deposited to the Open Science Framework database [https://osf.io/gf5wd/?view_only=d10bfe8438984bafa4e3c7909b2ecc30].

Acknowledgements:

This work is supported in part by the Clinical and Translational Proteomics Service Center at the University of Texas Health Science Center at Houston.

Disclosure and competing interests statement:

The authors declare that they have no conflict of interest

References:

Abu-Remaileh M, Wyant GA, Kim C, Laqtom NN, Abbasi M, Chan SH, Freinkman E, Sabatini DM (2017) Lysosomal metabolomics reveals V-ATPase- and mTOR-dependent regulation of amino acid efflux from lysosomes. *Science* 358: 807-813

An H, Ordureau A, Paulo JA, Shoemaker CJ, Denic V, Harper JW (2019) TEX264 Is an Endoplasmic Reticulum-Resident ATG8-Interacting Protein Critical for ER Remodeling during Nutrient Stress. *Mol Cell* 74: 891-908 e810

Bains H, Singh R (2021) Isolation of autophagic fractions from mouse liver for biochemical analyses. *STAR Protoc* 2: 100730

Cai Y, Saiyin H, Lin Q, Zhang P, Tang L, Pan X, Yu L (2005) Identification of a new RTN3 transcript, RTN3-A1, and its distribution in adult mouse brain. *Brain Res Mol Brain Res* 138: 236-243

Chen WW, Freinkman E, Wang T, Birsoy K, Sabatini DM (2016) Absolute Quantification of Matrix Metabolites Reveals the Dynamics of Mitochondrial Metabolism. *Cell* 166: 1324-1337 e1311

Chino H, Hatta T, Natsume T, Mizushima N (2019) Intrinsically Disordered Protein TEX264 Mediates ER-phagy. *Mol Cell* 74: 909-921 e906

Dikic I, Elazar Z (2018) Mechanism and medical implications of mammalian autophagy. *Nat Rev Mol Cell Biol* 19: 349-364

Ding WX, Yin XM (2012) Mitophagy: mechanisms, pathophysiological roles, and analysis. *Biol Chem* 393: 547-564

Escobar KA, Cole NH, Mermier CM, VanDusseldorp TA (2019) Autophagy and aging: Maintaining the proteome through exercise and caloric restriction. *Aging Cell* 18: e12876

Grumati P, Morozzi G, Holper S, Mari M, Harwardt MI, Yan R, Muller S, Reggiori F, Heilemann M, Dikic I (2017) Full length RTN3 regulates turnover of tubular endoplasmic reticulum via selective autophagy. *Elife* 6

Guan Y, Drake JC, Yan Z (2019) Exercise-Induced Mitophagy in Skeletal Muscle and Heart. *Exerc Sport Sci Rev* 47: 151-156

Hansen M, Chandra A, Mitic LL, Onken B, Driscoll M, Kenyon C (2008) A role for autophagy in the extension of lifespan by dietary restriction in C. elegans. *PLoS Genet* 4: e24

He C, Bassik MC, Moresi V, Sun K, Wei Y, Zou Z, An Z, Loh J, Fisher J, Sun Q *et al* (2012) Exercise-induced BCL2-regulated autophagy is required for muscle glucose homeostasis. *Nature* 481: 511-515

Khaminets A, Heinrich T, Mari M, Grumati P, Huebner AK, Akutsu M, Liebmann L, Stolz A, Nietzsche S, Koch N *et al* (2015) Regulation of endoplasmic reticulum turnover by selective autophagy. *Nature* 522: 354-358

Kirkin V, Lamark T, Johansen T, Dikic I (2009) NBR1 cooperates with p62 in selective autophagy of ubiquitinated targets. *Autophagy* 5: 732-733

Klionsky DJ, Petroni G, Amaravadi RK, Baehrecke EH, Ballabio A, Boya P, Bravo-San Pedro JM, Cadwell K, Cecconi F, Choi AMK *et al* (2021) Autophagy in major human diseases. *EMBO J* 40: e108863

Koyama-Honda I, Itakura E, Fujiwara TK, Mizushima N (2013) Temporal analysis of recruitment of mammalian ATG proteins to the autophagosome formation site. *Autophagy* 9: 1491-1499

Laker RC, Drake JC, Wilson RJ, Lira VA, Lewellen BM, Ryall KA, Fisher CC, Zhang M, Saucerman JJ, Goodyear LJ *et al* (2017) Ampk phosphorylation of Ulk1 is required for targeting of mitochondria to lysosomes in exercise-induced mitophagy. *Nat Commun* 8: 548

Lamark T, Johansen T (2021) Mechanisms of Selective Autophagy. *Annu Rev Cell Dev Biol* 37: 143-169

Levine B, Kroemer G (2019) Biological Functions of Autophagy Genes: A Disease Perspective. *Cell* 176: 11-42

Liu Y, Nguyen PT, Wang X, Zhao Y, Meacham CE, Zou Z, Bordieanu B, Johanns M, Vertommen D, Wijshake T *et al* (2020) TLR9 and beclin 1 crosstalk regulates muscle AMPK activation in exercise. *Nature* 578: 605-609

Martens S, Fracchiolla D (2020) Activation and targeting of ATG8 protein lipidation. *Cell Discov* 6: 23

Mizushima N, Yamamoto A, Matsui M, Yoshimori T, Ohsumi Y (2004) In vivo analysis of autophagy in response to nutrient starvation using transgenic mice expressing a fluorescent autophagosome marker. *Mol Biol Cell* 15: 1101-1111

Mochida K, Nakatogawa H (2022) ER-phagy: selective autophagy of the endoplasmic reticulum. *EMBO Rep* 23: e55192

Morishita H, Mizushima N (2019) Diverse Cellular Roles of Autophagy. *Annu Rev Cell Dev Biol* 35: 453-475

Morselli E, Maiuri MC, Markaki M, Megalou E, Pasparaki A, Palikaras K, Criollo A, Galluzzi L, Malik SA, Vitale I *et al* (2010) Caloric restriction and resveratrol promote longevity through the Sirtuin-1-dependent induction of autophagy. *Cell Death Dis* 1: e10

Murakawa T, Yamaguchi O, Hashimoto A, Hikoso S, Takeda T, Oka T, Yasui H, Ueda H, Akazawa Y, Nakayama H *et al* (2015) Bcl-2-like protein 13 is a mammalian Atg32 homologue that mediates mitophagy and mitochondrial fragmentation. *Nat Commun* 6: 7527

Nieto-Torres JL, Leidal AM, Debnath J, Hansen M (2021) Beyond Autophagy: The Expanding Roles of ATG8 Proteins. *Trends Biochem Sci* 46: 673-686

Pankiv S, Alemu EA, Brech A, Bruun JA, Lamark T, Overvatn A, Bjorkoy G, Johansen T (2010) FYCO1 is a Rab7 effector that binds to LC3 and PI3P to mediate microtubule plus end-directed vesicle transport. *J Cell Biol* 188: 253-269

Pena-Martinez C, Rickman AD, Heckmann BL (2022) Beyond autophagy: LC3-associated phagocytosis and endocytosis. *Sci Adv* 8: eabn1702

Pleiner T, Tomaleri GP, Januszyk K, Inglis AJ, Hazu M, Voorhees RM (2020) Structural basis for membrane insertion by the human ER membrane protein complex. *Science* 369: 433-436

Reid DW, Nicchitta CV (2012) Primary role for endoplasmic reticulum-bound ribosomes in cellular translation identified by ribosome profiling. *J Biol Chem* 287: 5518-5527

Rogov VV, Nezis IP, Tsapras P, Zhang H, Dagdas Y, Noda NN, Nakatogawa H, Wirth M, Mouilleron S, McEwan DG *et al* (2023) Atg8 family proteins, LIR/AIM motifs and other interaction modes. *Autophagy Rep* 2

Schaaf MB, Keulers TG, Vooijs MA, Rouschop KM (2016) LC3/GABARAP family proteins: autophagy-(un)related functions. *FASEB J* 30: 3961-3978

Schreml W, Burka ER (1968) Properties of membrane-bound ribosomes in reticulocytes. *J Biol Chem* 243: 3573-3580

Shevchenko A, Loboda A, Ens W, Schraven B, Standing KG, Shevchenko A (2001) Archived polyacrylamide gels as a resource for proteome characterization by mass spectrometry. *Electrophoresis* 22: 1194-1203

Tian W, Alsaadi R, Guo Z, Kalinina A, Carrier M, Tremblay ME, Lacoste B, Lagace D, Russell RC (2020) An antibody for analysis of autophagy induction. *Nat Methods* 17: 232-239

Wei Y, Chiang WC, Sumpter R, Jr., Mishra P, Levine B (2017) Prohibitin 2 Is an Inner Mitochondrial Membrane Mitophagy Receptor. *Cell* 168: 224-238 e210

Wyant GA, Abu-Remaileh M, Frenkel EM, Laqtom NN, Dharamdasani V, Lewis CA, Chan SH, Heinze I, Ori A, Sabatini DM (2018) NUFIP1 is a ribosome receptor for starvation-induced ribophagy. *Science* 360: 751-758

Xiong J, He J, Xie WP, Hinojosa E, Ambati CSR, Putluri N, Kim HE, Zhu MX, Du G (2019) Rapid affinity purification of intracellular organelles using a twin strep tag. *J Cell Sci* 132

Yao J, Jia L, Feathers K, Lin C, Khan NW, Klionsky DJ, Ferguson TA, Zacks DN (2016) Autophagy-mediated catabolism of visual transduction proteins prevents retinal degeneration. *Autophagy* 12: 2439-2450

Yao J, Qiu Y, Jia L, Zacks DN (2019) Autophagosome immunoisolation from GFP-LC3B mouse tissue. *Autophagy* 15: 341-346

Zaffagnini G, Savova A, Danieli A, Romanov J, Tremel S, Ebner M, Peterbauer T, Sztacho M, Trapannone R, Tarafder AK *et al* (2018) p62 filaments capture and present ubiquitinated cargos for autophagy. *EMBO J* 37

Zhang L, Li J, Ouyang L, Liu B, Cheng Y (2016) Unraveling the roles of Atg4 proteases from autophagy modulation to targeted cancer therapy. *Cancer Lett* 373: 19-26

Zhang Z, Wang Y, Ding Y, Hattori M (2020) Structure-based engineering of anti-GFP nanobody tandems as ultra-high-affinity reagents for purification. *Sci Rep* 10: 6239

Figure Legends

Fig 1. A novel method for isolating LC3B-positive autophagosomes from the tissues of GFP-LC3 mice. (A) Schematic illustration of the isolation process. Briefly, the tissues or cells are homogenized to release the cellular contents including cytosolic unlipidated GFP-LC3 (I) and autophagosomes containing lipidated GFP-LC3 (II). The lysates are then subjected to Size Exclusion Chromatography (SEC), during which process the large-sized autophagosomes are eluted earlier than the small-sized soluble GFP-LC3 I. Afterwards, the SEC fractions that contain autophagosomes are used for immunoaffinity-pull-down of autophagosomes using GFP nanobody-conjugated magnetic beads. **(B)** Western blots analysis shows the distribution of GFP-LC3 I and II, LC3 I and II, p62, ATG5 and p-ATG16L1 Ser 278 in different SEC fractions of skeletal muscle lysate obtained from a starved GFP-LC3 mouse. The fraction numbers, ranging from 1 to 21, indicate the elution order from earliest to latest, corresponding to the largest to smallest sizes. Fractions 1 to 6 which contain mature autophagosomes are used for isolation. Similar results were observed in at least three independent experiments. **(C)** Left**,** western blots analysis shows the enrichment of GFP-LC3 II, LC3 II and p62 in the autophagosomes preparation from the skeletal muscles of a starved GFP-LC3 mouse compared to that from a WT control. Similar results were observed in at least three independent experiments. Right, western blots analysis shows the levels of GFP-LC3 II and LC3 II in the SEC elutes of WT and GFP-LC3 muscle lysates before and after autophagosome isolation. The isolation efficiency was determined by calculating the depletion of GFP-LC3 II after isolation relative to the total amount of GFP-LC3 II present before isolation based on the results from three independent experiments. **(D)** Transmission Electron Microscope (TEM) images show the presence of autophagosomes with double membranes in the autophagosome preparations.

Fig 2. Autophagy cargo profiles in skeletal muscle during starvation and exercise. (A) The identification of proteins in the autophagosome preparations from skeletal muscle under basal, starvation and exercise conditions. In each biological replicate for each condition, proteins that are at least 1.5 times more abundant in the autophagosome preparations from the GFP-LC3 muscles than the corresponding WT control muscles are considered as “from autophagosomes. Each oval stands for one replicate, and the number near it indicates how

many proteins are identified as “from autophagosomes” in this replicate. The number in the overlapping region indicates the common proteins identified in all four replicates that are significantly more abundant in GFP-LC3 samples compared to WT samples ($p \leq 0.05$). These proteins were subjected to further analysis in (B) and (C). **(B)** The modified pie charts illustrate the percentage of proteins from a specific cytoplasmic component relative to the total number of proteins identified in the isolated autophagosomes under basal, starvation and exercise conditions. The number in the parentheses indicates how many proteins are from the specific cytoplasmic component. Proteins that are localized to multiple components were counted for each of their respective localizations. Thus, the sum of the percentages of all cytoplasmic components is more than 100%, and the pie charts are only approximate to reflect the portions. Refer to the values on the chart for accurate assessment. **(C)** The total abundance of proteins from various cellular components identified in the isolated autophagosomes under basal, starvation and exercise conditions. The abundance of proteins is normalized to the abundance of LC3B in each replicate. Proteins that are localized to multiple components are counted for each of their respective localizations. * $p < 0.05$, ** $p < 0.01$, *** $p < 0.001$ when compared to basal condition. $ $p < 0.05$, $$ $p < 0.01$, $$$ $p < 0.001$ when compared to exercise condition. Two sides, unpaired Student’s t-test was used for statistical analysis. Data are mean ± s.e.m.

Fig 3. Potential contribution of TEX264 and FAM134B to the elevated ER-phagy during starvation. (A) (B) Co-immunoprecipitation of FAM134B with GFP-LC3 II in skeletal muscle lysates from WT and GFP-LC3 mice (post SEC to eliminate GFP-LC3 I) shows more interaction between these two molecules under starvation condition than exercise condition. **(A)** representative blots. **(B)** quantification of the results from two independent experiments. Data points are individual mice (n = 5). **(C) (D)** Co-immunoprecipitation of GFP-LC3 II with TEX264 in skeletal muscles lysates from GFP-LC3 mice (post SEC to eliminate GFP-LC3 I) shows more interaction between these two molecules under starvation condition than exercise condition. **(C)** representative blots. **(D)** quantification of the results from two independent experiments. Data points are individual mice (n = 4). ** $p < 0.01$ using two sides, unpaired Student’s t-test. Data are mean ± s.e.m.

Fig EV1. Comparing the autophagosome isolation efficiency using tandem GFP nanobody and single GFP nanobody. (A) Purified single GFP nanobody and tandem GFP nanobody detected in the stain-free gel. Different amounts of purified proteins were loaded**. (B)** Western blot analysis shows increased enrichment of GFP-LC3 II, LC3 II, and p62 in autophagosome preparations from skeletal muscles of starved GFP-LC3 mice when using tandem GFP nanobody-conjugated beads compared to single GFP nanobody-conjugated beads during the pull-down step. Similar results were observed in at least three independent experiments.

Fig EV2. Autophagosome isolation from cell lines that express GFP-LC3. (A) (B) Autophagosome isolation were performed in HeLa cells **(A)** and MIA Paca-2 cells **(B)** that express GFP-LC3 or an empty vector as non-specific binding control. Western blot analysis shows enrichment of GFP-LC3 II, LC3 II, and p62 in autophagosome preparations from GFP-LC3 expressing cells (starved for 3 hours using Earle's Balanced Salt Solution) compared to those from control cells. Similar results were observed in at least three independent experiments.

Fig EV3. Autophagosome isolation from the skeletal muscles of GFP-LC3 mice under basal, starvation and exercise conditions. (A) Left, western blot analysis shows the levels of

lipidated GFP-LC3 II in skeletal muscles lysates from WT and GFP-LC3 mice (post SEC to eliminate GFP-LC3 I) under basal, starvation and exercise conditions. Calnexin and total protein levels determined by the staining signals from the stain-free gel were used as the loading controls. Right, quantification of GFP-LC3 II levels normalized to the stain-free signals as shown on the left (n=3). **(B)** Western blot analysis shows the enrichment of GFP-LC3 II, LC3 II, and p62 in the autophagosome preparations from the skeletal muscles of GFP-LC3 mice compared to those from WT mice under basal, starvation and exercise conditions. ** p <0.01, *** p < 0.001 when compared to basal condition. Two sides, unpaired Student's t-test was used for statistical analysis. Data are mean ± s.e.m.

Fig EV4. Autophagosomes from the skeletal muscle under starvation condition contain a higher abundance of ER proteins compared to those obtained under basal or exercise condition. On the right side of the graph, the abundance of SERCAs and Calsequestrin-1 identified in the isolated autophagosomes under basal, starvation and exercise conditions are shown. Notably, these proteins were not identified under basal nor exercise condition, thus the abundance values are zero. On the left side of the graph, the abundance of all ER proteins, excluding SERCAs and Calsequestrin-1, identified in the isolated autophagosomes under basal, starvation and exercise conditions is shown. The abundance of proteins is normalized to the abundance of LC3B protein in each replicate. * p < 0.05, *** p < 0.001 when compared to basal condition. $$$ p < 0.001 when compared to exercise condition. Two sides, unpaired Student's t-test was used for statistical analysis. Data are mean ± s.e.m.

Fig EV5. The abundance of proteins from various cellular components in the tissue lysates of skeletal muscle under basal, starvation and exercise conditions. (A) The identification of proteins in the tissue lysates of skeletal muscle under basal, starvation and exercise conditions. Each circle stands for one replicate, and the number near it indicates how many proteins were identified in this replicate. The number in the overlapping region is the number of proteins identified in all three replicates. These proteins were subjected to further analysis in (B). **(B)** The total abundance of proteins identified in (A) from various cellular components under basal, starvation and exercise conditions. The total protein abundance in each replicate was considered as 100. Proteins that are localized to multiple components were counted for each of their respective localizations. * p < 0.05, ** p <0.01, *** p < 0.001 when compared to basal condition. $$ p < 0.01 when compared to starvation condition. Two sides, unpaired Student's t-test was used for statistical analysis. Data are mean ± s.e.m.

Figure 1

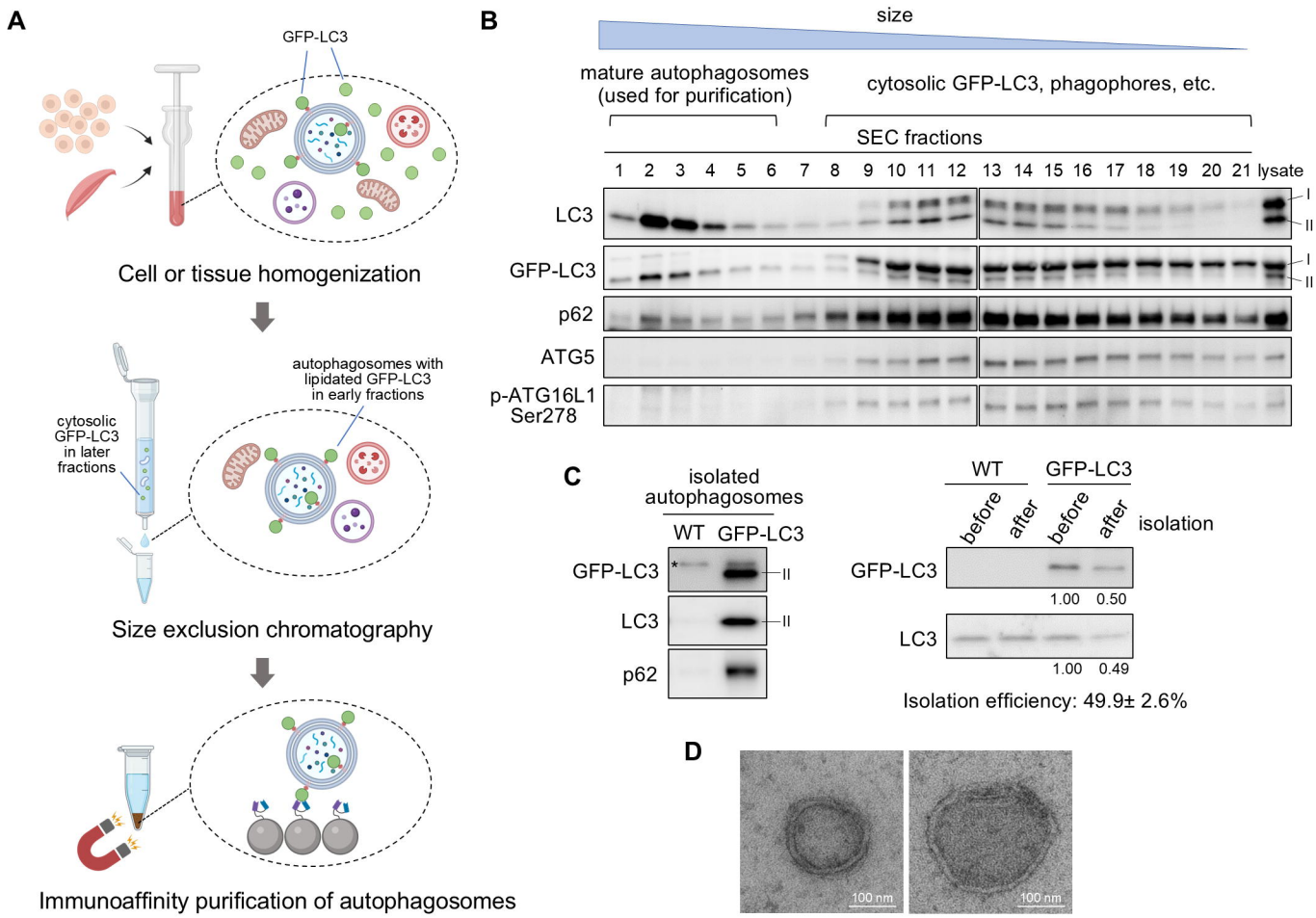
A
GFP-LC3
Cell or tissue homogenization
autophagosomes with lipidated GFP-LC3 in early fractions
cytosolic GFP-LC3 in later fractions
Size exclusion chromatography
Immunoaffinity purification of autophagosomes
B
size
mature autophagosomes (used for purification)
cytosolic GFP-LC3, phagophores, etc.
SEC fractions
1 2 3 4 5 6 7 8 9 10 11 12 13 14 15 16 17 18 19 20 21 lysate
LC3
GFP-LC3
p62
ATG5
p-ATG16L1 Ser278
I
II
C
isolated autophagosomes
WT GFP-LC3
GFP-LC3
LC3
p62
WT GFP-LC3
before after before after isolation
1.00 0.50
1.00 0.49
Isolation efficiency: 49.9± 2.6%
D
100 nm
100 nm

Figure 2

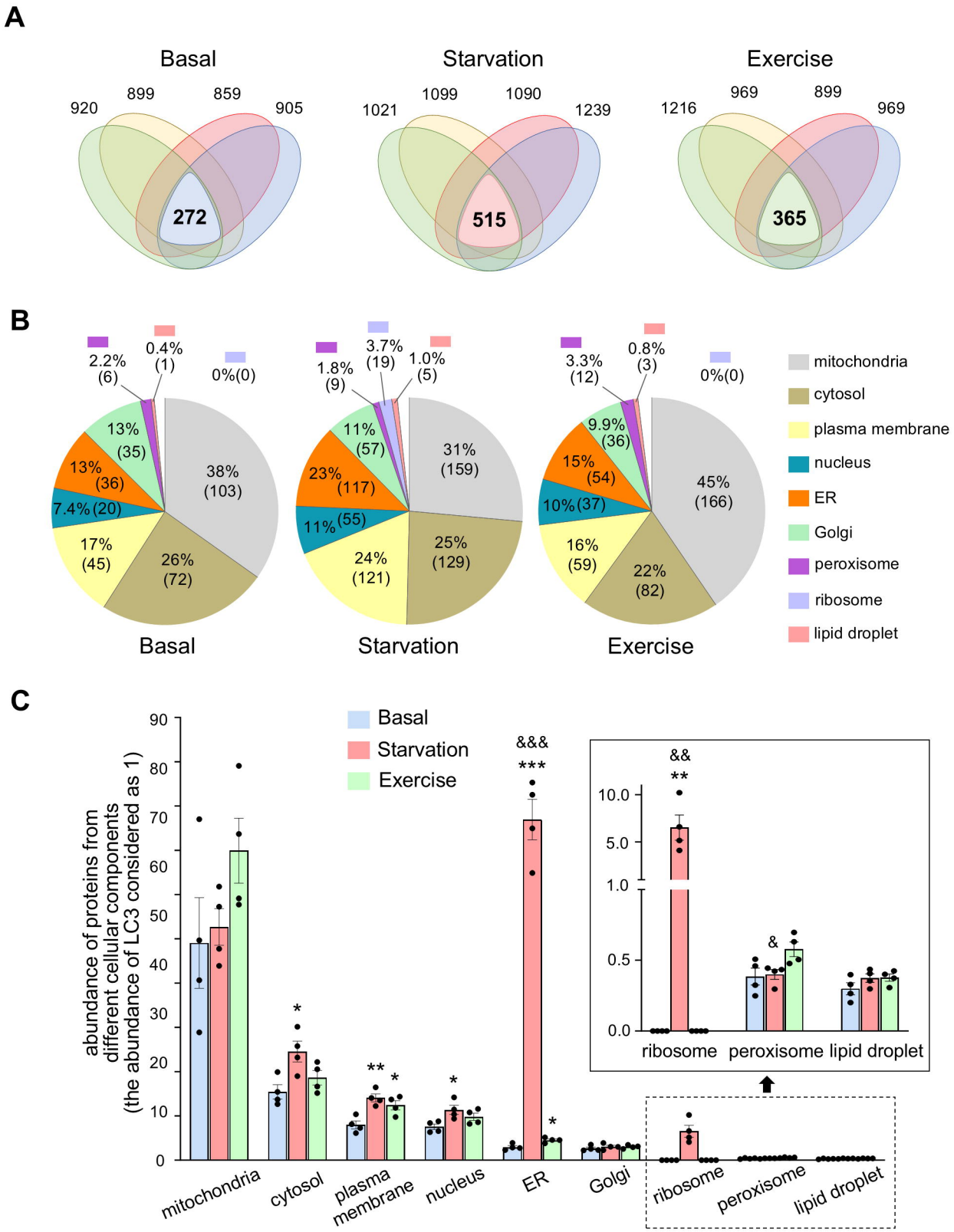
A
Basal
920
899
859
905
272
Starvation
1021
1099
1090
1239
515
Exercise
1216
969
899
969
365
B
2.2% (6)
0.4% (1)
0%(0)
13% (35)
13% (36)
7.4% (20)
17% (45)
26% (72)
38% (103)
Basal
1.8% (9)
3.7% (19)
1.0% (5)
11% (57)
23% (117)
11% (55)
24% (121)
25% (129)
31% (159)
Starvation
3.3% (12)
0.8% (3)
0%(0)
9.9% (36)
15% (54)
10% (37)
16% (59)
22% (82)
45% (166)
Exercise
mitochondria
cytosol
plasma membrane
nucleus
ER
Golgi
peroxisome
ribosome
lipid droplet
C
Basal
Starvation
Exercise
abundance of proteins from different cellular components (the abundance of LC3 considered as 1)
90
80
70
60
50
40
30
20
10
0
&&&
***
*
**
*
*
*
mitochondria
cytosol
plasma membrane
nucleus
ER
Golgi
ribosome
peroxisome
lipid droplet
&&
**
10.0
5.0
1.0
0.5
0.0
&
ribosome
peroxisome
lipid droplet

Figure 3

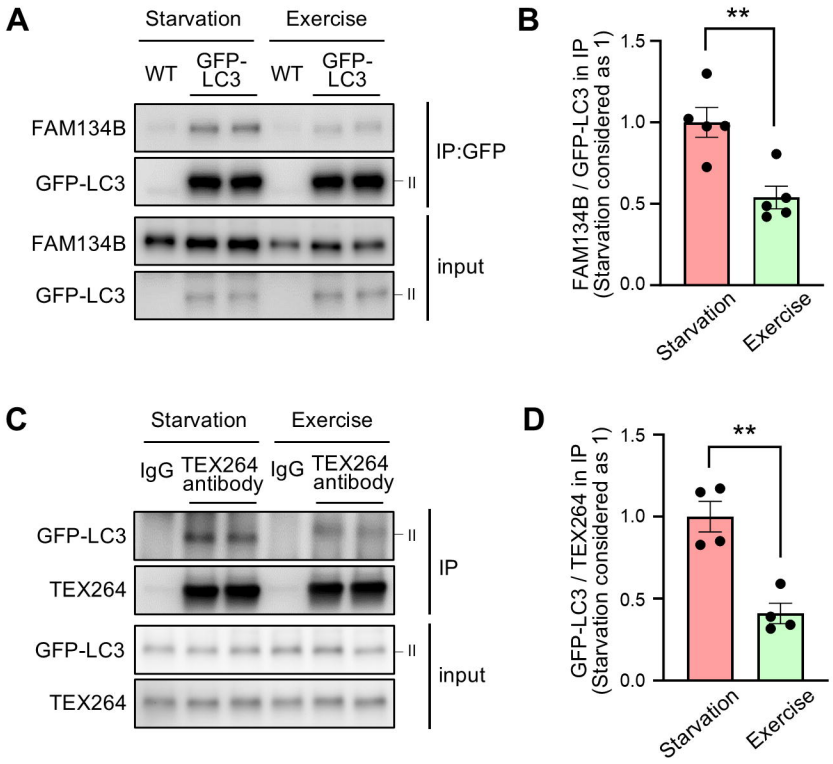
A
Starvation
Exercise
WT
GFP-LC3
WT
GFP-LC3
FAM134B
GFP-LC3
II
IP:GFP
FAM134B
GFP-LC3
II
input
B
**
FAM134B / GFP-LC3 in IP
(Starvation considered as 1)
1.5
1.0
0.5
0.0
Starvation
Exercise
C
Starvation
Exercise
IgG
TEX264 antibody
IgG
TEX264 antibody
GFP-LC3
II
TEX264
IP
GFP-LC3
II
TEX264
input
D
**
GFP-LC3 / TEX264 in IP
(Starvation considered as 1)
1.5
1.0
0.5
0.0
Starvation
Exercise

Figure EV1

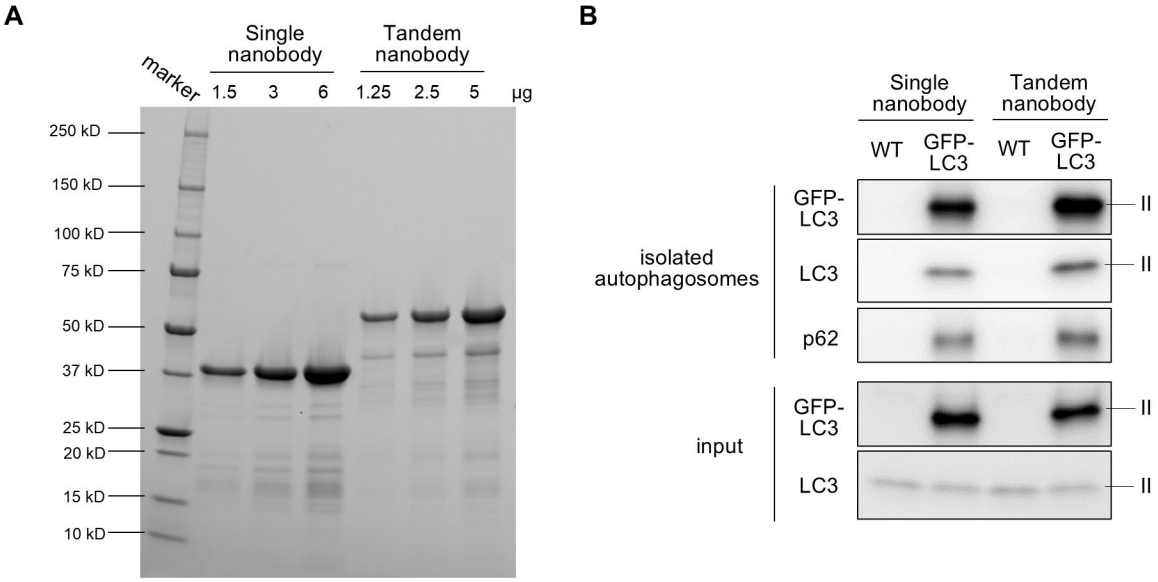
A
Single nanobody
Tandem nanobody
marker
1.5
3
6
1.25
2.5
5
µg
250 kD
150 kD
100 kD
75 kD
50 kD
37 kD
25 kD
20 kD
15 kD
10 kD
B
Single nanobody
Tandem nanobody
WT
GFP-LC3
WT
GFP-LC3
isolated autophagosomes
GFP-LC3
LC3
p62
input
GFP-LC3
LC3
II
II
II
II

Figure EV2

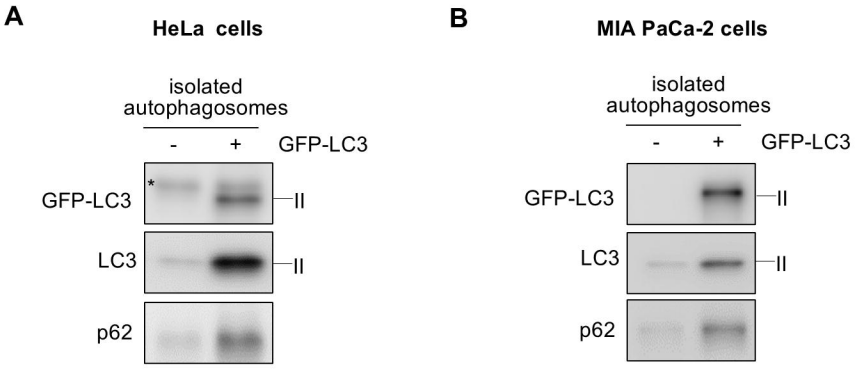
A
HeLa cells
isolated autophagosomes
-
+
GFP-LC3
GFP-LC3
*
II
LC3
II
p62
B
MIA PaCa-2 cells
isolated autophagosomes
-
+
GFP-LC3
GFP-LC3
II
LC3
II
p62

Figure EV3

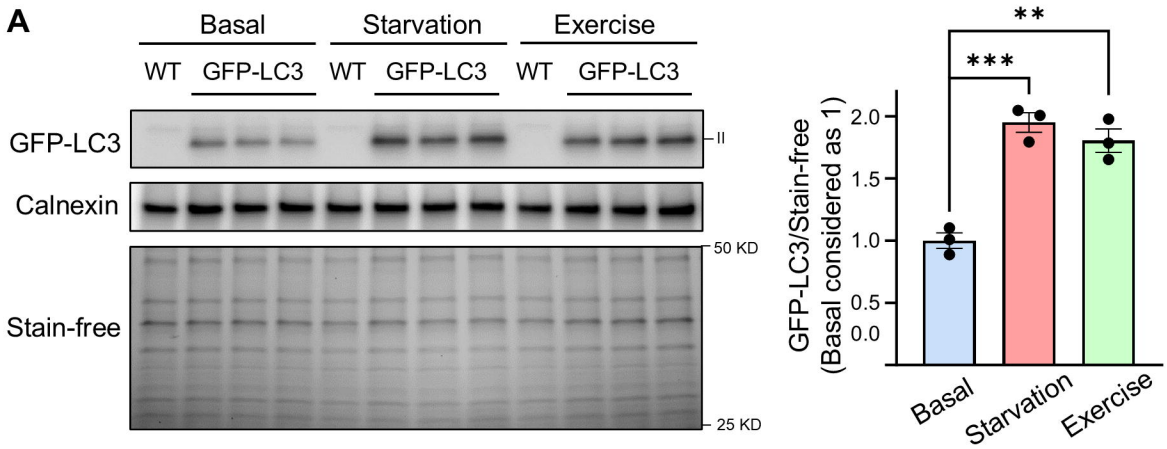
A
Basal
Starvation
Exercise
WT
GFP-LC3
WT
GFP-LC3
WT
GFP-LC3
GFP-LC3
Calnexin
Stain-free
II
50 KD
25 KD
**
***
GFP-LC3/Stain-free
(Basal considered as 1)
2.0
1.5
1.0
0.5
0.0
Basal
Starvation
Exercise

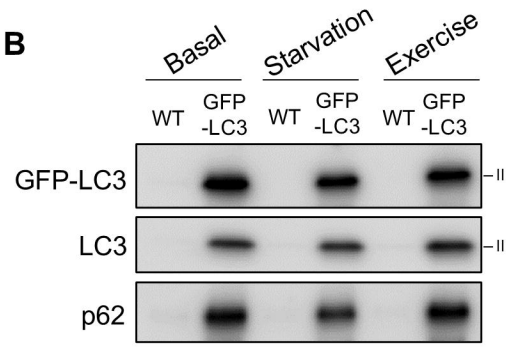
B
Basal
Starvation
Exercise
WT
GFP -LC3
WT
GFP -LC3
WT
GFP -LC3
GFP-LC3
LC3
p62
II
II

Figure EV4

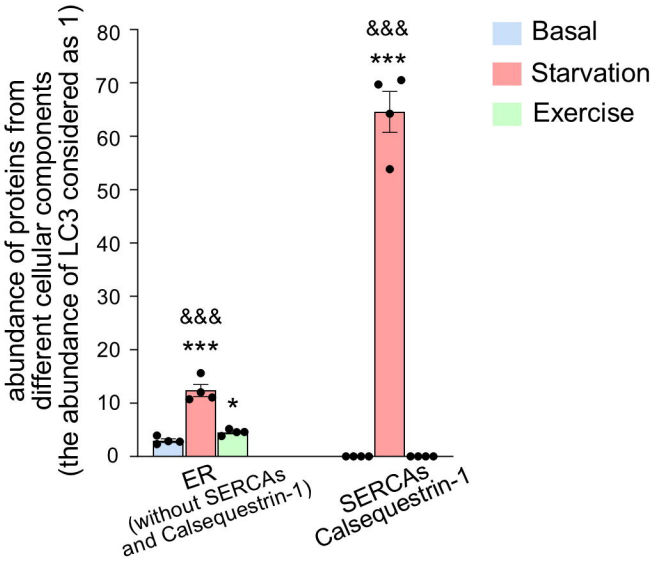
abundance of proteins from different cellular components (the abundance of LC3 considered as 1)
80
70
60
50
40
30
20
10
0
&&&
***
*
&&&
***
ER (without SERCAs and Calsequestrin-1)
SERCAs Calsequestrin-1
Basal
Starvation
Exercise

Figure EV5

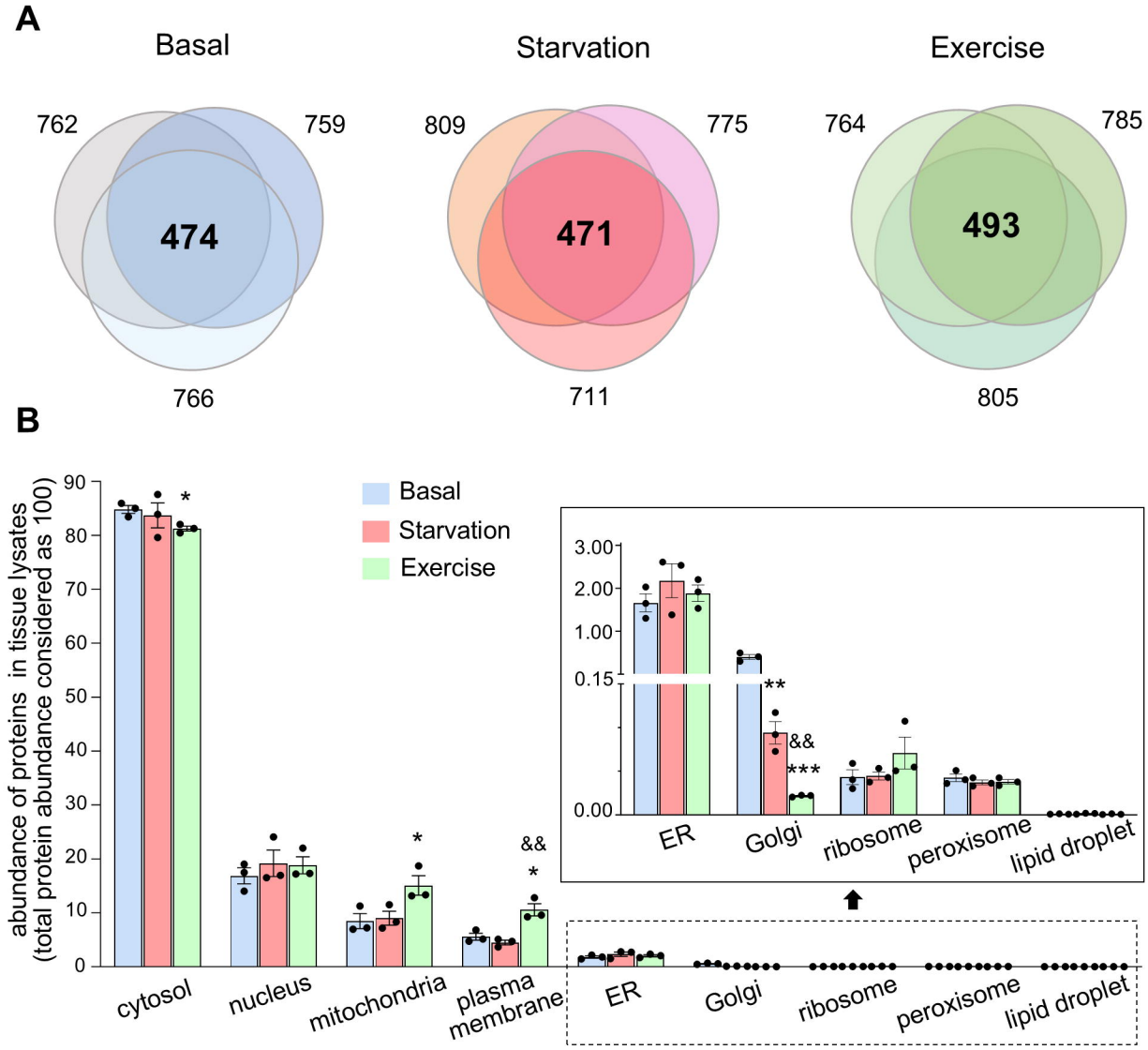
A
Basal
Starvation
Exercise
762
759
474
766
809
775
471
711
764
785
493
805
B
Basal
Starvation
Exercise
abundance of proteins in tissue lysates
(total protein abundance considered as 100)
90
80
70
60
50
40
30
20
10
0
*
*
&&
*
cytosol
nucleus
mitochondria
plasma membrane
3.00
2.00
1.00
0.15
0.00
**
&&
***
ER
Golgi
ribosome
peroxisome
lipid droplet